Mon. Not. R. Astron. Soc. **344,** 385–398 (2003)

The *Hubble Deep Field* North SCUBA Super-map – I. Submillimetre maps, sources and number counts

Colin Borys,[1,2★] Scott Chapman,[2] Mark Halpern[1] and Douglas Scott[1]

[1]*Department of Physics & Astronomy, University of British Columbia, Vancouver, BC, Canada*
[2]*California Institute of Technology, Pasadena, CA 91125, USA*

Accepted 2003 May 15. Received 2003 May 14; in original form 2003 February 21

ABSTRACT

We investigate the emission of submillimetre-wave radiation from galaxies in a 165 arcmin^2 region surrounding the *Hubble Deep Field* North. The data were obtained from dedicated observing runs from our group and others using the SCUBA camera on the James Clerk Maxwell Telescope (JCMT), and combined using techniques specifically developed for low signal-to-noise ratio source recovery. The resulting 'Super-map' is derived from approximately 60 shifts of JCMT time, taken in a variety of observing modes and chopping strategies, and combined here for the first time. At 850 μm we detect 19 sources at $>4\sigma$, including five not previously reported. We also list an additional 15 sources between 3.5 and 4.0σ (where two are expected by chance). The 450-μm map contains five sources at $>4\sigma$. We present a new estimate of the 850- and 450-μm source counts. The number of submillimetre galaxies we detect account for approximately 40 per cent of the 850-μm submillimetre background, and we show that mild extrapolations can reproduce it entirely. A clustering analysis fails to detect any significant signal in this sample of SCUBA-detected objects. A companion paper describes the multiwavelength properties of the sources.

Key words: methods: numerical – methods: statistical – galaxies: formation – large-scale structure of Universe – submillimetre.

1 INTRODUCTION

The *Hubble Deep Field* North (HDF-N) (Williams et al. 1996), a small region of the sky targeted by the *Hubble Space Telescope* (*HST*), has stimulated the study of the high-redshift Universe ever since the data were released in 1995. The original optical image of the HDF is one of the deepest ever obtained, and resolves thousands of galaxies in an area of a few arcmin^2. However, since optical images capture only a narrow part of the spectrum, and since the rest-frame wavelength range detected depends on the redshift, it is necessary to supplement the *HST* image with data at other wavelengths in order to obtain a more complete understanding of galaxy evolution. In the years since the HDF image became public, deep pointings using radio, X-ray, near-infrared (IR) and mid-IR telescopes have been conducted. Additionally, optical spectroscopy has been carried out on hundreds of suitable objects in the field, thereby obtaining redshifts for most of the brighter *HST*-detected objects.

The original HDF field is the size of a single WFPC2 field of view, roughly 2 × 2 arcmin^2. *HST* also obtained shallower observations in fields adjacent to this, extending the region of study to roughly 6 × 6 arcmin^2. These 'flanking fields' have also been covered by other telescopes, and in fact over time the region associated with the HDF has been extended to approximately 10 × 10 arcmin^2 in most wavebands. For an excellent review of the HDF-N region and its impact on the optical view of astronomy, refer to the article by Ferguson, Dickinson & Williams (2000). Despite these extensive observations, fully understanding the high-redshift Universe is hindered by the presence of dust, which re-processes radiation and emits it in the far-infrared (FIR). The importance of this is clearly demonstrated in the population of galaxies detected by the Submillimetre Common User Bolometer Array (SCUBA; Holland et al. 1999). Even with the tremendous observational effort of the past 5 years, we have made only modest progress with SCUBA-detected galaxies beyond the conclusions drawn from the pioneering work of Hughes et al. (1998) and Smail, Ivison & Blain (1997). SCUBA mapping surveys have constrained the number counts, and show that significant evolution is required in the local ultraluminous infrared galaxy (ULIRG) population in order to explain the abundance of high-redshift SCUBA sources.

Having detected these sources, the goal now is to characterize them and try to answer fundamental questions concerning their nature. What powers their extreme luminosities? What is their redshift distribution? What objects do they correspond to today? One way to do this is by performing pointed photometry on a list of high-redshift sources detected at other wavelengths, but this obviously

★E-mail: borys@submm.caltech.edu

introduces some biases. An alternate approach, one taken by many groups, is to perform a 'blank field' survey, and compare the submillimetre map against images taken with other telescopes at other wavelengths. Arguably, the best field to do this is in the Hubble Deep Field region, which has more telescope time invested in observations than any other extragalactic deep field. In addition to the data already available, observations with the *HST*-ACS and upcoming confusion-limited *SIRTF* observations, make this an appealing region to target with SCUBA. For all of these reasons it is worthwhile to combine the available submillimetre data in this part of the sky.

2 OBSERVATIONS

Observations with SCUBA require the user to 'chop' the secondary mirror at a rate of 7.8125 Hz between the target position and a reference (also called 'off') position. The difference between the signals measured at each position removes common-mode atmospheric noise. The direction and size of the chop throw is adjustable, and is typically set such that the off position does not change over time due to sky rotation. A map made in such a way will then exhibit a negative copy of the source in the off position.

In raster-scan mode, the whole telescope moves on the sky in order to sample a region larger than the array size. A map made from data collected in this mode is commonly referred to as a 'scan-map'. An alternative way to sample a large area is to piece together smaller 'jiggle' maps. In this mode, the telescope stares toward the target and the secondary mirror steps around a dither pattern designed to fill in the space on the image plane between the conical feedhorns. Photometry mode is very similar to jiggle-mapping, except the dither pattern is smaller in order to spend more time observing the target object. The trade off is that the image plane is not fully sampled, and there will be gaps in a map made from photometry data. Jiggle-mapping and photometry also differ from scan mapping because they use two off positions in the chopping process. Therefore, there will be two negative echoes of each source.

Our group has produced a shallow 'scan-map' of the region at 450 and 850 μm (Borys et al. 2002, hereafter Bo02) using SCUBA. Given the high profile of the region, however, groups from the UK and Hawaii also targeted the HDF to exploit the rich multiwavelength observations available. The $\sim 3 \times 3$ arcmin^2 area centred on the HDF itself, studied originally by Hughes et al. (1998, hereafter H98), was recently re-analysed by Serjeant et al. (2003, hereafter S02) and we use their published data for comparison here. Results from observations taken by the Hawaii group can be found in Barger, Cowie & Richards (2000, hereafter Ba00). We have obtained all of these data from the James Clerk Maxwell Telescope (JCMT) archive or from the observers directly and embedded them in our scan-map. The extra data considerably increase the sensitivity of the final map in the overlap regions, but at the expense of much more inhomogeneous noise and a correspondingly more complicated data analysis. Co-adding data taken in different observing modes has not previously been performed for extragalactic submillimetre surveys, and so we discuss our procedure in some detail below.

The full list of projects allocated time to study the HDF region is extensive. Observing details for each project are given in Table 1. Almost all work carried out in the region has used the jiggle-map mode in deep, yet small surveys. Three projects involved targeted photometry observations taken in 'two-bolometer chopping' mode. The SURF User Reduction Facility (SURF; Jenness & Lightfoot 1998) software was not able to process these particular files for inclusion in the map, but we shall discuss these observations later. Project M00BC01 is a single jiggle-map observation taken in such a way that co-adding it to the map is also difficult, and shall be described later as well. All of the remaining data could be co-added into a 'Super-map', as we now describe.

Table 1. Summary of SCUBA HDF region observations. Type refers to either photometry (P), jiggle-map (J) or scan-map (S). Approximate 1σ noise estimates in mJy are provided, though they do vary somewhat across the individual images. The area surveyed in arcmin^2 is also listed. Projects denoted by an asterisk were photometry observations that could not be added directly to the map, due to the inability of SURF to extract the bolometer positions for two-bolometer chopping observations. In addition, M00BC01 was taken using an unfortunate chopping configuration which cancelled out two sources near the western edge of the map. These data are not folded directly into the map. In total, there have been almost 60 shifts (of 8 h each) in which the telescope was observing this region, which is considerably more than the original *HST* optical imaging.

Project ID	Type	Shifts	σ_{450} (mJy)	σ_{850} (mJy)	Area (arcmin^2)
M97BU65	P, J	17	4	0.4	9
M98AC37	P	2	65	2	3
M98AH06	P	4	11	1	3
M98BC30	S	2	75	6	160
M98BU61	P	1	33	3	2
M99AC29	S	2	95	6	160
M99AH05	J	11	20	2	39
M99BC41*	P	1	N/A	N/A	N/A
M99BC42	P, J, S	3	120	6	160
M00AC16*	P	1	N/A	N/A	N/A
M00AC21*	P	1	N/A	N/A	N/A
M00AH07	J	4	40	2	12
M00BC01	J	1	N/A	3	5
M01AH31	J	7	25	2	22

3 DATA REDUCTION

We start by simply regridding the bolometer data on to an output map, ignoring for a moment the effect of a strongly varying effective point spread function (PSF, i.e. the effect of the different chops) across the field. Fig. 1 demonstrates just how different the observations are. Shown is the PSF at various locations in the field, alongside the 850-μm noise map with contours overlaid. Because the telescope is moving at a rate of 3 arcsec per sample while taking scan-map data, there is no advantage to choosing a pixel size smaller than 3 arcsec. Some other studies have chosen smaller (1 arcsec) pixels for jiggle maps, but given the uncertainties in JCMT pointings, we feel that a choice of 3-arcsec pixels is sufficient.

3.1 Flux and pointing calibration

Registering the individual data sets with respect to each other is difficult, due to the lack of bright sources in the field. The pointing log for each night of data was inspected, and in all but a few cases there is no reason to distrust the pointing; pointing checks were always performed on the same side of the meridian as the HDF, and observations were not conducted through transit.[1] Although

[1] During much of the period in which these data were obtained, the JCMT telescope would drop slightly in elevation while tracking an object through transit.

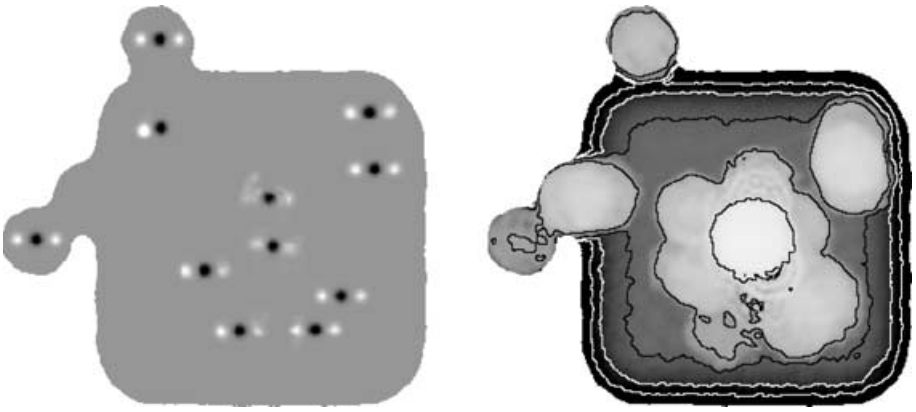

Figure 1. Layout of the SCUBA HDF observations. The majority of the data are contained within 12 × 12 arcmin^2 , but other jiggle maps were also taken within the wider *Chandra* or VLA images. The left-hand panel is a map of the HDF using simulated sources but the real pointing information. This allows the variable PSF to be easily seen. Here black corresponds to sources and white to the negative echoes caused by the necessity to chop. Various parts of the field were observed in different ways, as is evident from the different PSFs. On the right is the actual noise map at 850 μm with contours at 1, 3, 5, 7 and 9 mJy overlaid. The deepest pointings of Hughes et al. (1998) are in the centre of the image, while other jiggle maps and photometry observations can be seen superimposed on our scan-map. The corresponding images for the 450-μm map are very similar in appearance, though with higher noise levels.

individual night-to-night pointing comparisons between data sets is not feasible, it is still possible to check for a systematic pointing offset between scan and jiggle maps. One might be concerned about errors of the order of 3 arcsec, due to the speed at which the telescope moves while scanning.

In a map made solely from the scanning observations, a group of sources is detected that corresponds to the same objects seen in the deep jiggle map in Ba00 (project M99AH05). A least-squares comparison between a 4 × 4 arcmin^2 in the scan-map against the same area in the jiggle-map indicates a 4 ± 4 arcsec offset along the direction of the chop (110° east of north).

Exploiting the well-established FIR/radio correlation, we also performed a pointing check using the following procedure: we took a list of μJy VLA 1.4-GHz sources detected by Richards (2000) and extracted the 850-μm flux from the super-map at each position. The average of these fluxes was used as a figure of merit in checking the pointing. By shifting the super-map in both directions and calculating this 'stacked' flux, we find that no significant positional offset is required to maximize the average submillimetre flux at the radio positions.

For each night of jiggle-map and photometry observations, flux calibrations were performed on suitable targets in the area. In each case these calibrations were consistent with the averages determined for others taken in the same time periods, and with the larger sample reported in Archibald et al. (2002). Since individual calibrations may have a larger statistical variation, the average calibration value over the run was used instead.

Flux calibration of the scan maps is more problematic. Since this mode is currently not so well characterized, it is important to compare the map against those taken from the better understood jiggle maps. Although pointing seems well constrained, the fluxes in the HDF scan-map are generally larger than their jiggle-map counterparts when using the 'standard' gains. This was an issue first discussed in Bo02. Unfortunately, no usable scan-map calibration measurements were taken during the observations. Therefore, we proceed by adjusting the overall calibration of the scan-map and finding, in a chi-squared sense, the value that minimizes the difference between the two maps:

$$\chi^2(r) = \sum (S_{\rm jiggle} - r S_{\rm scan})^2, \quad (1)$$

where the sum is over all the pixels. Because the beam patterns (two- versus three-beam) are different, we use only those pixels within a beamwidth of the sources detected in the jiggle maps. Based on this analysis we determine that scan-map flux conversion factors are 0.8 times that of the standard jiggle-map calibrations.

We obtained scan-map calibration data for other (unrelated to HDF) projects that observed planets, and estimated the flux conversion factor from them. This analysis also obtains the factor of 0.8 difference between scan- and jiggle-map calibrations.

3.2 Source detection

No effort was made to deconvolve this combined map; the observing strategies employed by both our group and others do not interconnect pixels very well, and therefore a robust deconvolution cannot be performed. However, in order to gain back the extra sensitivity from the off-beams, we would like to fit each pixel in the map to the multibeam PSF. This procedure has been adopted by other groups as well, but the complication in this case is the variable PSF across the field.

Instead of fitting to the PSF, we can fold in the flux from the off-beams in a time-wise manner. For each sample, we add the measured flux to the pixel being pointed to in addition to its negative flux (appropriately weighted) at the position of the off-beam. This is equivalent to performing one iteration of the map-making procedure described in Johnstone et al. (2000, see also Borys 2002). A single Gaussian is then used to fit for sources in the final map. This requires an image relatively free of sources that might lie in the location of the off-beam of another source, but produces the same output as one would obtain from fitting with the beam pattern. The resulting image should be considered not so much as a map but rather the answer to the question: what is the best estimate of the flux of an isolated point source at the position of each pixel? The image can only be properly interpreted in conjunction with the accompanying noise map.

4 MONTE CARLO SIMULATIONS

There are several simulations that must be performed to assess the reliability of the maps. To determine how many detections might

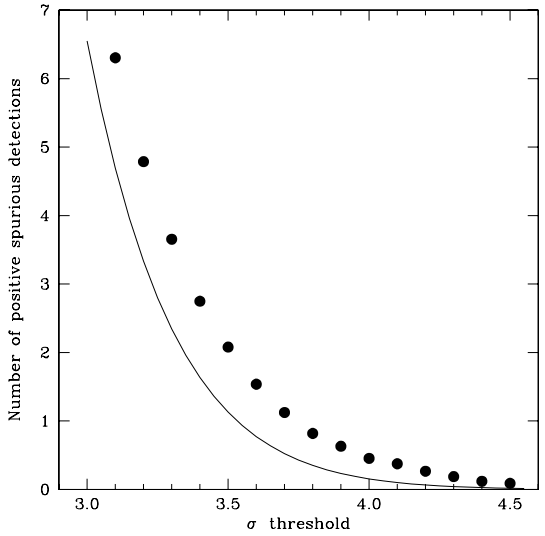

Figure 2. The number of positive sources in the 850-μm map expected at random. The filled circles show how many spurious sources were detected in simulated maps made from noise alone. Error bars are omitted for clarity, but are small because of the large number of sources generated in the many simulations. The number of positive sources one would expect by chance given Gaussian statistics and a Gaussian-shaped beam with a FWHM of 14.7 arcsec in an 165 arcmin^2 region is plotted as the thick line.

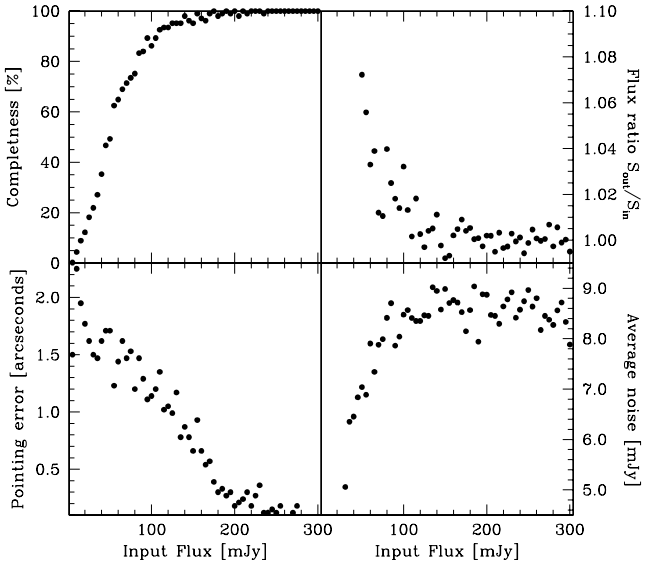

Figure 3. 450-μm source recovery Monte Carlo results. From left to right and top to bottom the plots are: (a) completeness; (b) flux bias ratio; (c) pointing error; and (d) noise level. Error bars are not plotted for clarity, but one can gauge the uncertainty by the scatter of the points in the vertical direction.

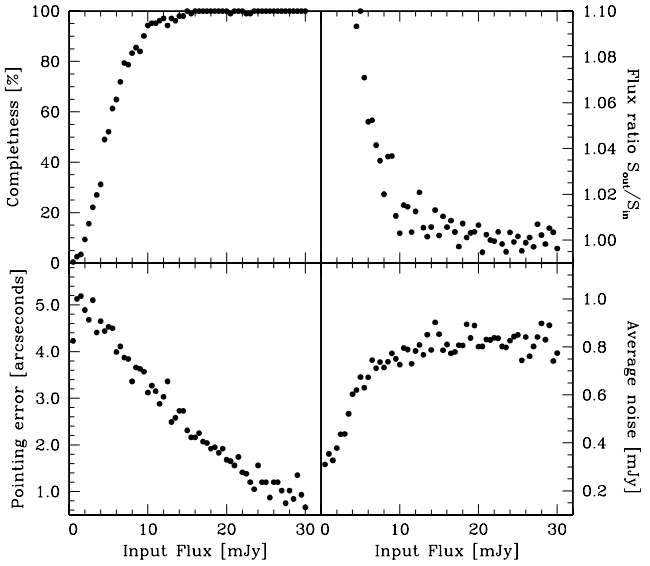

Figure 4. 850-μm source recovery Monte Carlo results. The order is the same as in the previous figure. In general, the plots are very similar to their 450-μm counterparts, with fluxes being an order of magnitude smaller.

be false positives, we created a map by replacing the 850-μm data with Gaussian random noise with a variance equivalent to the noise estimated for each bolometer. The map was then run through the same source-finder algorithm as the real data. This was repeated 100 times. The average number of positive and negative detections as a function of signal-to-noise (S/N) ratio threshold is plotted in Fig. 2, along with the number one would expect based simply on Gaussian statistics and the number of independent beam sizes in the map (which is an underestimate because it assumes well-behaved noise). A 3.5σ cut is commonly used, but these results suggest that at this threshold approximately four detections will be spurious in our map (two positive and two negative detections). Given that the slope of this plot is still rather steep at 3.5σ, small errors in the noise estimate can lead to more false positives. Therefore, we adopt a 4.0σ cut to determine sources in the HDF super-map. Note that the number of false positives for the 450-μm map will be four times larger because the beam is half as big (of course if the noise is not well behaved this could be even worse!). Therefore, one wants to set a high detection threshold for 450-μm objects (but as we will find later, there is only one $>5\sigma$ source at 450 μm). The situation is further complicated by the fact that the true background is not blank, and is populated by many unresolved sources that create confusion noise.

To further estimate the reliability of our detections, we added 500 sources (one at a time) of known flux for a range of flux levels into the map and attempted to extract them using the same pipeline as for the real data. A source was considered 'recovered' if it was detected with an S/N ratio greater than 4.0 and its position was within half the FWHM of the input position. At each input flux, the position offset, flux bias and noise of all the recovered sources were averaged and plotted in Figs 3 and 4 for the 450- and 850-μm maps, respectively.

The panel showing completeness is self-explanatory; it plots the percentage of sources recovered in the Monte Carlo simulations as a function of input flux. As one expects, it is difficult to recover faint sources around the noise limit, but very bright sources are always recovered. We will discuss this issue more when deriving source counts.

The ratio of output and input flux in the adjacent panel shows that sources fainter than the threshold have been scattered up due to the presence of noise and are 'detected' with higher than their true flux. The relevant noise components in this case are instrumental noise and confusion noise. The latter is called Eddington bias (Eddington 1940), and dominates the central part of the map where the instrumental noise is smallest. At 850 μm, the confusion limit is ∼1 mJy, and thus sources with instrumental noise around this level will be subject to Eddington bias.

The rms of the difference between input and output positions allows us to estimate a positional error for real detections as a function of flux level. As one would expect, the uncertainty is smaller as the input flux goes up. The final plot in the sequence shows the average noise level associated with the recovered sources as a function of input flux. At the faint end, the noise is lower because such sources are only detected in the deepest parts of the map. As the flux of the source increases above the noise level of the least sensitive region (in this case the underlying scan-map), the average noise of the detections levels off to the average noise level of the field. The 450-μm plots (Fig. 3) are very similar to those at 850 μm (Fig. 4), scaled by approximately a factor of 10 in flux.

Basic conclusions at 850 μm are that at a flux limit of 8 mJy the source counts are approximately 80 per cent complete, fluxes are biased by only a few per cent, and positions are accurate to approximately 3.5 arcsec. The brighter objects are constrained much better than this, but there are few of them. At the faintest levels confusion has a significant effect on fluxes, positions and completeness.

5 SUBMILLIMETRE SOURCES IN THE HDF

Most of the 850-μm sources exhibit off-beam signatures that are distinguishable by eye (the negative echoes to the left and right of the sources). Finding sources at 450 μm, however, is more difficult. The single beam pattern is not well described by a Gaussian, plus the sensitivity at 450 μm is too poor to detect any but the brightest sources. In addition, being more weather-dependent, the noise is even more inhomogeneous than for the 850-μm data. Nevertheless, we will report the 3σ upper limit to the 450-μm flux for each 850-μm detection. To avoid reporting spurious detections, we have set a threshold of 4.0σ on the 850-μm catalogue derived from the super-map. However, a supplementary list of sources at 850 μm detected above 3.5σ is also provided for comparison against other data sets. The full list of 850- and 450-μm sources is presented in Table 2.

A simple test of source reality is to search for negative flux objects. All but two negative sources found were associated with the off-beam of one of our positive detections. Based on the Monte Carlo simulations, this is not unreasonable. There are 19 sources at 850 μm detected over 4σ, five of which are new, not having been reported before in the individual surveys. Apart from a few exceptional cases, described below, all sources previously reported in the region are recovered at comparable flux levels. An additional 15 sources are detected between 3.5σ and 4σ. Our Monte Carlo simulations suggest that on average two of these may be spurious. An image of the 850-μm super-map is given in Fig. 5. There are only five sources recovered from the 450-μm image, which is shown in Fig. 6. There have been no 450-μm detections previously reported in the HDF. The finder chart in Fig. 7 can be used to identify the sources extracted by our algorithm in each of the maps.

5.1 Comparing the source list against previous surveys

A plot comparing the recovered fluxes against those previously published is given in Fig. 8. We show the difference between the published fluxes and super-map estimates. The flux differences should be zero, and based on the size of the error bars it is clear that no significant variations exist between the estimates. The objects that appear slightly discrepant are discussed at length below, and all sources will be described in detail in a forthcoming paper. It should be noted that the error bars on the sources recovered from the super-map are generally smaller than those obtained from the individual submaps.

5.1.1 The central HDF region from Hughes/Serjeant et al.

Eight sources, labelled HDF850.1 to HDF850.8 are associated with the data collected by H98. The more thorough analysis in S02 found that one of them (HDF850.3) detected in the original map fails to meet new detection criteria. It is also the only source undetected in the super-map presented here. HDF850.4 and HDF850.5 appeared to be a blend of two sources in their original map, and therefore both H98 and SO2 took the extra step of attempting to fit the amplitude and position of them. With the super-map, however, this pair of sources is better fitted by a single source with flux comparable to the sum of fluxes from the two extracted by S02. This may be because we use larger pixels (3 arcsec compared with 1 arcsec from S02) and therefore lose some of the resolution required to separate adjacent objects. Sources HDF850.6 and HDF850.7 are detected at a fainter level than reported in S02. These discrepancies might be partly due to their positions – both are in a noisier region of the individual submap, and near its edge. The super-map contains additional data (especially photometry) in the central HDF region, and so one would expect our noise estimates to be mildly lower compared with those of S02, which is indeed generally true.

5.1.2 HDF flanking field jiggle maps from Barger et al.

The seven sources detected individually in Ba00 are confirmed in the super-map at comparable flux levels except for one object not detected in the radio band. This is most probably due to differences in analysis methods; Ba00 used aperture photometry with annuli centred on radio positions believed to be associated with the submillimetre detection. The source in question had no counterpart, and therefore determining flux with aperture photometry is not as straightforward. Even when the submap alone is considered individually, the measured flux does not match that originally reported.

5.1.3 Scan-map observations of Borys et al.

All six sources from the 4σ list of Bo02 are recovered, although two of them are detected at lower significance in the super-map. Four of the six sources from the supplementary list of 3.5σ sources are not recovered in the super-map. Three of these exist in regions of overlap between surveys. This supports the warning made in Bo02 that 4σ SCUBA detections are less likely to be spurious than lower S/N ratio ones. In general, however, we find that sources detected at $>4\sigma$ are confirmed in separate submaps. This is an important test of the reliability of faint SCUBA detections, which can only be effectively carried out in the HDF region, because of the overlapping independent data sets.

5.2 Comparison with photometry observations

As we have mentioned, a number of photometry observations taken in the two-bolometer chopping mode were conducted. Although these data sets cannot be co-added into the map, we can compare flux estimates for the photometry bolometer with the position in the super-map.

Table 2. Submillimetre detections in the HDF super-map. Only sources with an S/N ratio (shown in parentheses) greater than 3.5 are listed. If the source was previously detected in a separate survey, then the reference to the paper is given, and the measured flux from there. The papers are Ba00, Bo02, S02. 3σ upper limits in the other channel are given for each source.

ID	RA	Dec.	$S_{850} \pm \sigma_{850}$	$S_{450} \pm \sigma_{450}$	Previously detected
			850-μm detections $\geqslant 4\sigma$		
SMMJ123607+621145	12:36:07.3	62:11:45	$15.2 \pm 3.8(4.0\sigma)$	<97	Bo02: 15.4 ± 3.4 mJy
SMMJ123608+621251	12:36:08.5	62:12:51	$16.0 \pm 3.7(4.3\sigma)$	<95	Bo02: 13.8 ± 3.3 mJy
SMMJ123616+621518	12:36:16.6	62:15:18	$6.3 \pm 0.9(6.5\sigma)$	<35	
SMMJ123618+621009	12:36:18.9	62:10:09	$6.6 \pm 1.5(4.3\sigma)$	<66	
SMMJ123618+621554	12:36:18.7	62:15:54	$7.2 \pm 0.9(8.1\sigma)$	<34	Ba00: 7.8 ± 1.6 mJy
SMMJ123621+621254	12:36:21.8	62:12:54	$12.1 \pm 2.6(4.7\sigma)$ 9	<85	Bo02: 11.4 ± 2.8 mJy
SMMJ123621+621712	12:36:21.3	62:17:12	$8.8 \pm 1.56.0\sigma$	<72	Ba00: 7.5 ± 2.3 mJy
					Bo02: 13.2 ± 2.9 mJy
SMMJ123622+621618	12:36:22.6	62:16:18	$8.6 \pm 1.0(8.5\sigma)$	<45	Ba00: 7.1 ± 1.7 mJy
SMMJ123634+621409	12:36:34.2	62:14:09	$11.2 \pm 1.6(7.1\sigma)$	<67	Ba00: 19.0 ± 2.8 mJy
SMMJ123637+621157	12:36:37.3	62:11:57	$7.0 \pm 0.8(8.3\sigma)$	<46	
SMMJ123646+621451	12:36:46.3	62:14:51	$8.5 \pm 1.3(6.4\sigma)$	<47	Ba00: 10.7 ± 2.1 mJy
					Bo02: 11.4 ± 2.9 mJy
SMMJ123650+621318	12:36:50.6	62:13:18	$2.0 \pm 0.4(5.3\sigma)$	<11	S02: HDF850.4/5 2.1 ± 0.3 mJy
SMMJ123652+621227	12:36:52.3	62:12:27	5.9 ± 0.3 (18.0σ)	<12	S02: HDF850.1 5.6 ± 0.4 mJy
SMMJ123656+621203	12:36:56.6	62:12:03	$3.7 \pm 0.4(8.8\sigma)$	<16	S02: HDF850.2 3.5 ± 0.5 mJy
SMMJ123700+620912	12:37:00.4	62:09:12	$8.6 \pm 2.1(4.1\sigma)$	<85	Ba00: 11.9 ± 3.0 mJy
SMMJ123701+621148	12:37:01.3	62:11:48	$4.0 \pm 0.8(5.2\sigma)$	<27	S02: HDF850.6 6.4 ± 1.7 mJy
SMMJ123703+621303	12:37:03.0	62:13:03	$3.4 \pm 0.6(5.3\sigma)$	<25	
SMMJ123707+621412	12:37:07.7	62:14:12	$9.9 \pm 2.5(4.0\sigma)$	<85	
SMMJ123713+621206	12:37:13.3	62:12:06	$6.1 \pm 1.4(4.3\sigma)$	<40	Ba00: 8.8 ± 2.0 mJy
			Additional 850-μm detections $\geqslant 3.5\sigma$ and $<4.0\sigma$		
SMMJ123607+621021	12:36:07.3	62:10:21	$13.5 \pm 3.7(3.7\sigma)$	<97	
SMMJ123608+621433	12:36:08.5	62:14:33	$6.1 \pm 1.7(3.6\sigma)$	<60	
SMMJ123611+621215	12:36:11.9	62:12:15	$12.8 \pm 3.4(3.7\sigma)$	<90	Bo02: 12.2 ± 3.0 mJy
SMMJ123628+621048	12:36:28.7	62:10:48	$4.4 \pm 1.2(3.7\sigma)$	<55	
SMMJ123635+621239	12:36:35.6	62:12:39	$3.0 \pm 0.8(3.6\sigma)$	<41	S02: HDF850.7 5.5 ± 1.5 mJy
SMMJ123636+620700	12:36:36.9	62:07:00	$22.1 \pm 5.6(3.9\sigma)$	<155	
SMMJ123648+621842	12:36:48.0	62:18:42	$19.5 \pm 5.4(3.6\sigma)$	<154	
SMMJ123652+621354	12:36:52.7	62:13:54	$1.8 \pm 0.4(3.9\sigma)$	<16	S02: HDF850.8 1.7 ± 0.5 mJy
SMMJ123653+621121	12:36:53.1	62:11:21	$2.8 \pm 0.8(3.6\sigma)$	<40	
SMMJ123659+621454	12:36:59.1	62:14:54	$5.2 \pm 1.4(3.8\sigma)$	<72	
SMMJ123706+621851	12:37:06.9	62:18:51	$21.6 \pm 5.8(3.8\sigma)$	<178	
SMMJ123719+621109	12:37:19.7	62:11:09	$7.2 \pm 2.0(3.6\sigma)$	<55	
SMMJ123730+621057	12:37:30.4	62:10:57	$13.3 \pm 3.6(3.7\sigma)$	<98	Bo02: 14.3 ± 3.2 mJy
SMMJ123731+621857	12:37:31.0	62:18:57	$27.1 \pm 7.6(3.6\sigma)$	<286	
SMMJ123741+621227	12:37:41.6	62:12:27	$23.7 \pm 6.1(3.9\sigma)$	<185	
			450-μm detections $>4\sigma$		
SMMJ123619+621127	12:36:19.3	62:11:27	<5.8	$110 \pm 26(4.2\sigma)$	
SMMJ123632+621542	12:36:32.9	62:15:42	<5.9	$105 \pm 25(4.2\sigma)$	
SMMJ123702+621009	12:37:02.6	62:10:09	<5.2	$120 \pm 27(4.4\sigma)$	
SMMJ123727+621042	12:37:27.4	62:10:42	<10.4	$220 \pm 42(5.2\sigma)$	
SMMJ123743+621609	12:37:43.8	62:16:09	<24.0	$300 \pm 72(4.2\sigma)$	

We should also note that while the scan-map observations were being taken, several photometry observations were conducted at positions of tentative detections in order to verify them. None of these positions correspond to detections in the final map, but all have fluxes consistent with the corresponding position in the super-map. This illustrates that the practice of picking out low S/N ratio sources 'by eye' in SCUBA surveys is not very effective. Our group has also conducted two observing programmes designed to understand the submillimetre properties of Lyman-break galaxies (LBGs, Chapman et al. 2000) and optically faint radio sources (OFRS, Chapman et al. 2002). These types of source will be discussed further in Paper II. Three measured LBGs that fall within the region of the HDF are not detected in either the photometry measurements or the super-map. Of the seven OFRS photometry measurements, all have comparable fluxes at their corresponding position in the super-map. A summary plot similar to that shown previously when comparing known detections is given in Fig. 9. Again, no significant discrepancies exist between the estimates.

6 NUMBER COUNTS OF SUBMILLIMETRE SOURCES

In order to estimate the density of sources brighter than some flux threshold S, $N(>S)$ from our list of detected sources in Table 2, we must account for several anticipated statistical effects.

(i) The threshold for source detection, $S_{\rm T} = m\sigma$ is not uniform because the noise varies dramatically across the map.

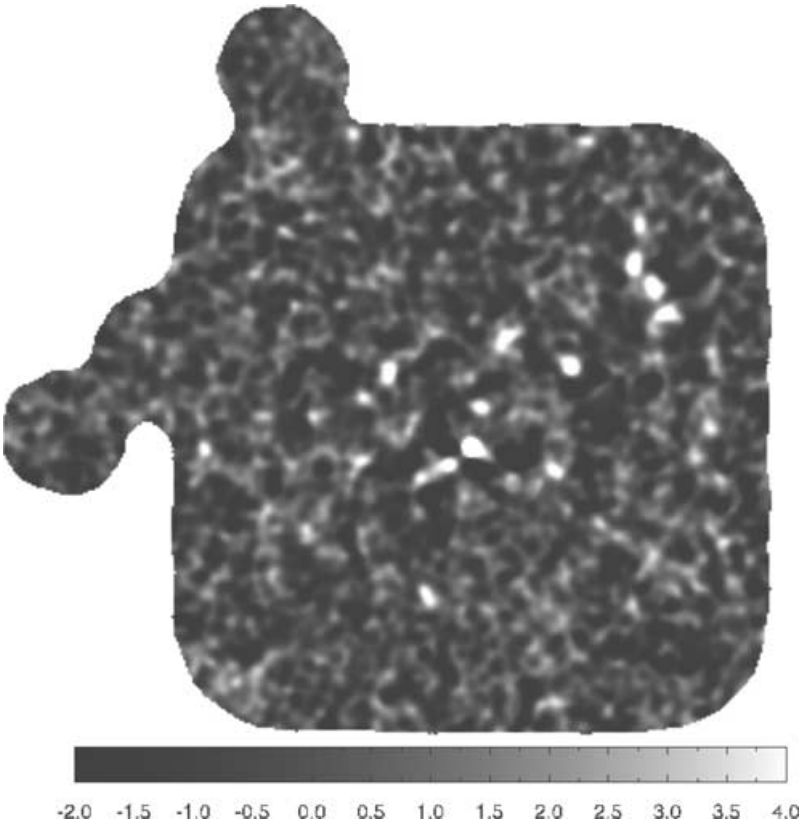

Figure 5. The 850-μm signal-to-noise ratio map. The grey-scale is stretched to highlight sources. This image can be used in conjunction with the finder chart in Fig. 7 to identify the objects reported in the source list.

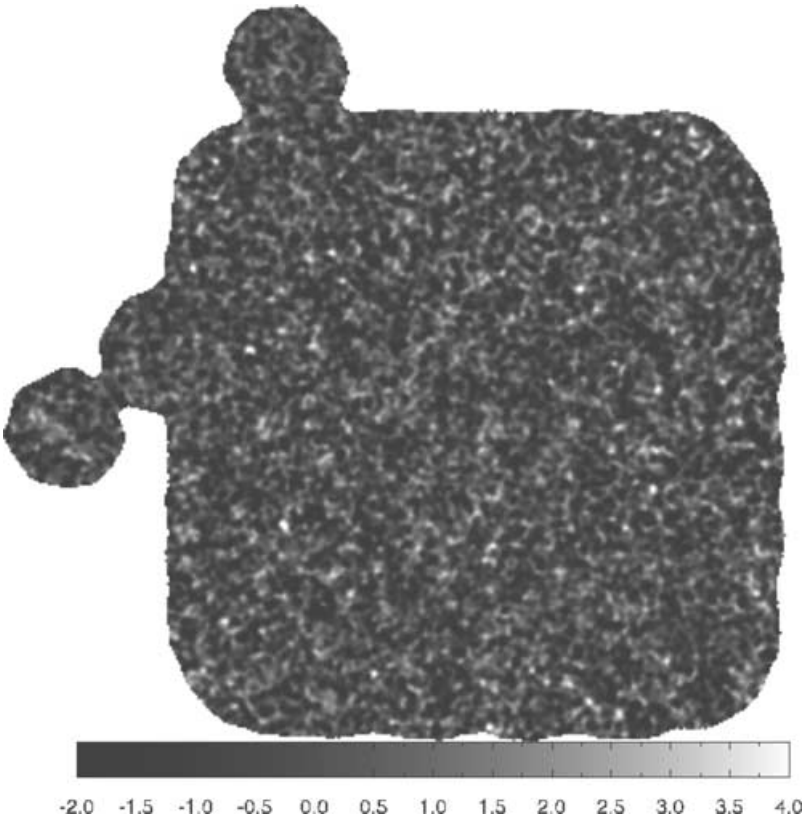

Figure 6. The 450-μm signal-to-noise ratio map. The grey-scale is stretched to highlight sources.

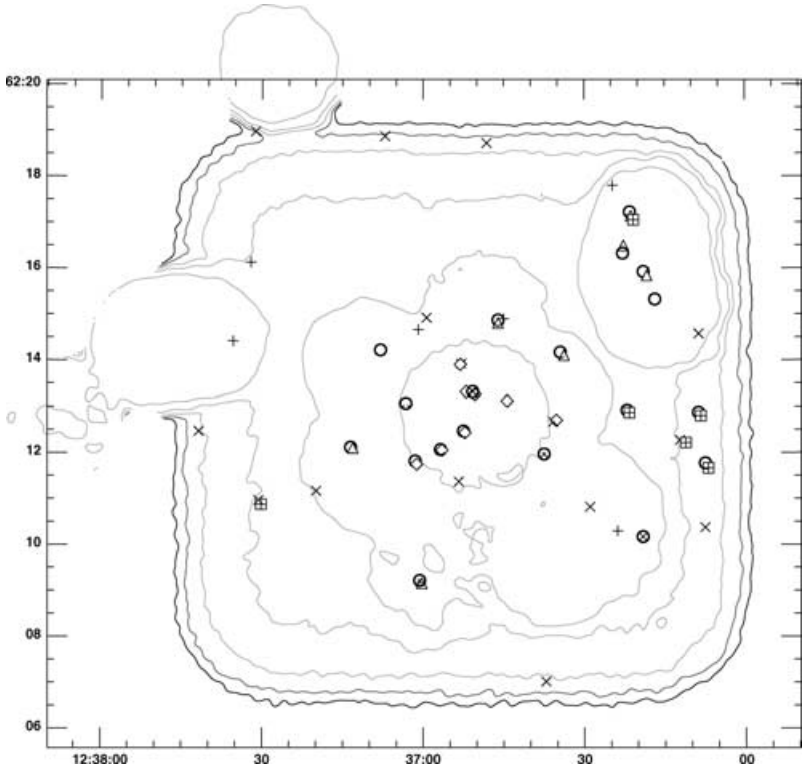

Figure 7. Finder chart for submillimetre sources detected in the HDF super-map. The outlines are 850-μm noise contour levels from 1 to 11 mJy (darkest) in steps of *2* mJy. Triangles are 850-μm source positions from Barger et al. (2000), diamonds from S02, squares with an embedded plus are the 4σ sources from Borys et al. (2002), and the plus symbols are the lower S/N ratio sources from that survey. Circles with crosses are sources recovered above 4σ from the super-map, and crosses show those additional sources detected at lower significance. The five 450-μm sources detected in the super-map are denoted with asterisks.

(ii) As a result of confusion and detector noise, sources dimmer than $S_{\rm T}$ might be scattered above the detection threshold and claimed as detected.

(iii) Similarly, sources brighter than $S_{\rm T}$ might be missed because of edge effects, possible source overlaps and confusion.

Item (iii) is simply the completeness of our list of sources. For a source density $N(S)\,{\rm d}S$, which falls with increasing flux, the effect of item (ii) can exceed that from item (iii), resulting in an Eddington bias in the estimated source counts. One can calculate the ratio of the integrated source count to the number of sources detected using the 'detectability':

$$\frac{1}{\gamma(S')} = \frac{\int_{S'}^{\infty} N(S)\,{\rm d}S}{\int_{0}^{\infty} \phi(S,\,S')N(S)\,{\rm d}S}, \tag{2}$$

where $N(S)\,{\rm d}S$ is the number of sources with a flux between S and $S + {\rm d}S$. We have introduced the quantity $\phi(S,\,S')$, which is the fraction of sources between a flux, S and $S + {\rm d}S$, that are detected above a threshold, S'. Note that $\phi(S,\,S')$ ranges between zero and unity, but $1/\gamma(S')$ can be larger than unity, depending on the form of $N(S)$ and choice of S'. For bright sources, where the completeness is 1.0 and the S/N ratio is high, $\phi(S,\,S')$ should approach unity.

The numerator of equation (2) is the quantity we are trying to determine, and the denominator is the output from the survey. To determine $N(>S)$ we simply take the raw counts from our survey and multiply them by $\gamma(S')$. The calculation of $\gamma(S')$ from the Monte Carlo estimates of $\phi(S,\,S')$ requires a model of the source counts, of which there are many different forms in the literature. All share the property that they are steep at the bright end and shallow at the faint end. They are also typically constrained such that the total amount of energy does not exceed the measured value of the submillimetre extragalactic background. We employ the double power-law form described in Scott et al. (2002),

$$\frac{{\rm d}N(>S)}{{\rm d}S} = \frac{N_0}{S_0}\left[\left(\frac{S}{S_0}\right)^{\alpha} + \left(\frac{S}{S_0}\right)^{\beta}\right]^{-1}, \tag{3}$$

and use $S_0 = 1.8$ mJy, $\alpha = 1.0$, $\beta = 3.3$ and $N_0 = 1.5 \times 10^4$ deg^{-2}.

Our Monte Carlo simulations give us $\phi(S,\,S')$, which we fit using the form

$$\phi(S,\,S') = 1 - \exp[A(S - B)^C]. \tag{4}$$

for each value of S'. This was chosen empirically to match the shape of $\phi(S,\,S')$. An alternative approach would be to perform more Monte Carlo simulations with a finer spacing in ΔS and then spline the result to allow for interpolation between the sample points – the results are almost identical. Using these estimates of $\phi(S,\,S')$, together with the source-count model, $\gamma(S')$ can be computed numerically using equation (2).

The quantity γ relates what we want to determine, $N(>S)$, with the number of sources our survey detects. Obviously γ is influenced by what model is used in the calculation described above, and other forms of the source spectrum are found in the literature. We find γ varies by no more than 15 per cent across a wide range of reasonable

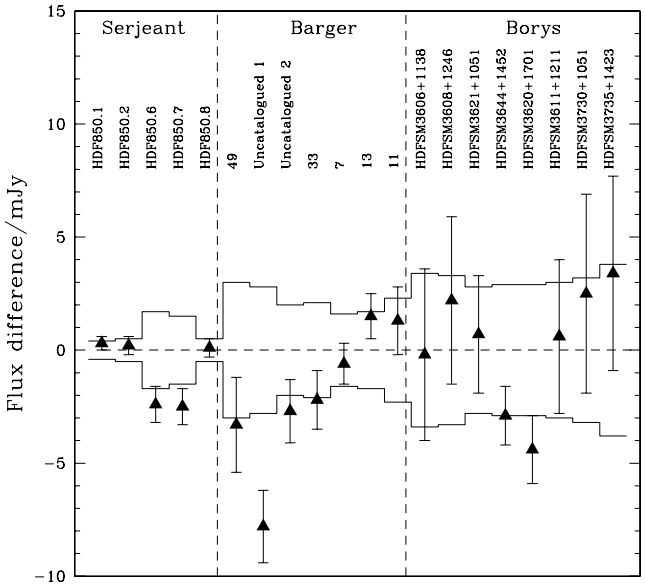

Figure 8. Our new source list compared with previously reported detections. We show the difference between previously reported flux and that derived here for each source in common. The outline denotes the size of the error bars from the previously reported estimates. We subtract the reported fluxes from our own, and plot the difference and error bar as the filled triangles. See the text for a more complete description for those few points that seem discordant.

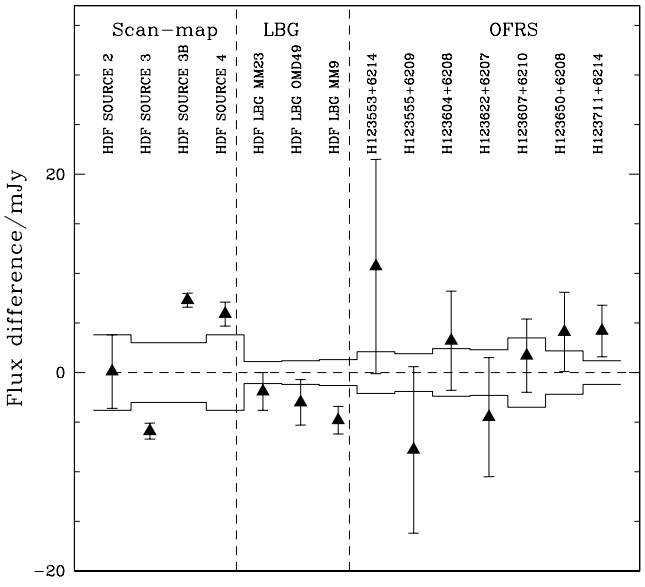

Figure 9. Comparing super-map fluxes with photometry estimates. We plot the difference between reported photometry fluxes from observations not added into the map and those derived from the super-map. As before, the outline shows the error bar from the reported values, while our points (after subtracting off the reported fluxes) are plotted as solid triangles. Since some of the photometry goes much deeper than our map, their error estimates are in those cases much lower. All sources are in reasonable agreement within the combined error bar of each estimate. Here, 'LBG' is a Lyman-break galaxy target and 'OFRS' is an optically faint radio source.

parameter values. This is smaller than the Poissonian error caused by having so few sources detected.

6.1 The 850-μm number counts

In Fig. 10 we plot the γ determined using the source count parameters described above, and $\phi(S, S')$ determined from the Monte Carlo simulations.

The detectability passes through unity at around 7 mJy; sources fainter than this are not detected very efficiently, and therefore we must boost the raw count to account for the incompleteness. Past this, brighter source counts obtain a slight boost from fainter sources that have been scattered above the threshold due to noise. Given $\gamma(S)$, we can now calculate the counts based on the number of sources detected in the entire 165 arcmin^2 super-map. This is given in tabular form (see Table 3) and as a plot alongside other estimates of the 850-μm source counts (in Fig. 11).

For the above source count approach we have provided estimates at a number of flux values (chosen to be integer numbers of mJy). There are other ways of presenting the counts, which avoid the need for binning. An alternative method uses the flux bias ratio (e.g. a smooth curve fitted to the bottom right-hand panel of Fig. 4) to transform the flux of each detected source, and then estimate the effective area in which such a source could have been detected. The results of this approach are shown by the step function plotted in Fig. 11, and are clearly consistent with the other estimate.

In general, the derived counts are in excellent agreement with estimates from other surveys. They also agree broadly with the input model used to estimate $\gamma(S)$. It should be noted that while other surveys use 68 per cent confidence bounds, we prefer to quote 95 per cent limits. It is interesting to note that the bright counts from

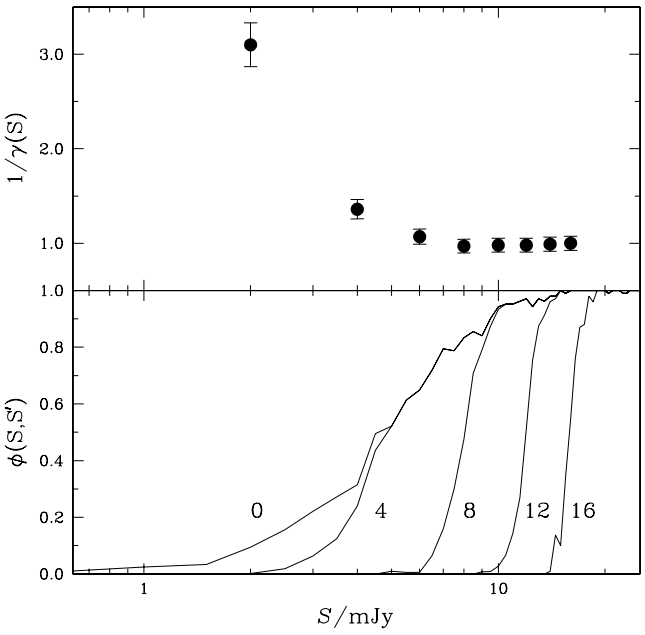

Figure 10. Summary of the 850-μm source-count calculation. In the top panel we plot the detectability, determined using the source-count model described in the text. As expected, it is higher at low flux levels (indicating that the survey has missed sources) and approaches unity at the bright end. Between 7 and 12 mJy the detectability is slightly lower than one, demonstrating that some sources below the threshold are contributing. The error bars represent the scatter obtained when using a range of source-count models that roughly fit the measured counts and submillimetre background. In the lower panel, we plot $\phi(S, S')$ for S' ranging from 0 to 16 mJy in steps of 4 mJy. The $S' = 0$ case is simply the completeness of the survey.

Table 3. 850-μm source counts from the HDF super-map using only the $\geqslant 4\sigma$ detections. The total area surveyed is 165arcmin^2, and the error ranges are 95 per cent confidence bounds on a Poisson distribution. We list results in steps of *2* mJy. We also include published results from other surveys for comparison. These include the comparable results from the wide area 8-mJy blank field survey, and three separate surveys conducted toward galaxy clusters, which appear to show a higher estimate than blank field counts.

S (mJy)	$N_{\rm raw}$ ($>S$)	$\gamma(S)$	$N(>S)$	$N_{8\,\rm mJy}$ ($>S$) (Scott et al. 2002)	$N_{\rm cluster}$ ($>S$) (Cowie et al. 2002)	$N_{\rm cluster}$ ($>S$) (Smail et al. 2002)	$N_{\rm cluster}$ ($>S$) (Chapman et al. 2002b)
0.25						51000^{+21000}_{-21000}	
0.3					33000^{+63000}_{-13000}		
0.5					18000^{+12000}_{-9000}	27000^{+10000}_{-10000}	
1					9000^{+14000}_{-5000}	9500^{+3400}_{-3400}	15000^{+5700}_{-3900}
2	19	3.10	1923^{+1002}_{-739}		3500^{+1500}_{-1000}	2900^{+1000}_{-1000}	6800^{+2600}_{-1900}
3							3560^{+1560}_{-1200}
4	16	1.36	710^{+409}_{-293}			1700^{+800}_{-800}	1800^{+990}_{-690}
5					2100^{+800}_{-300}		
6	14	1.07	489^{+304}_{-213}	550^{+100}_{-170}			1000^{+700}_{-450}
8	9	0.99	285^{+231}_{-149}	320^{+80}_{-100}		900^{+580}_{-580}	
10	4	0.98	128^{+173}_{-90}	180^{+60}_{-60}			360^{+770}_{-310}
12	3	0.98	96^{+157}_{-74}	40^{+30}_{-30}			
14	2	0.99	65^{+142}_{-55}				
16	1	1.00	33^{+121}_{-31}			<420	

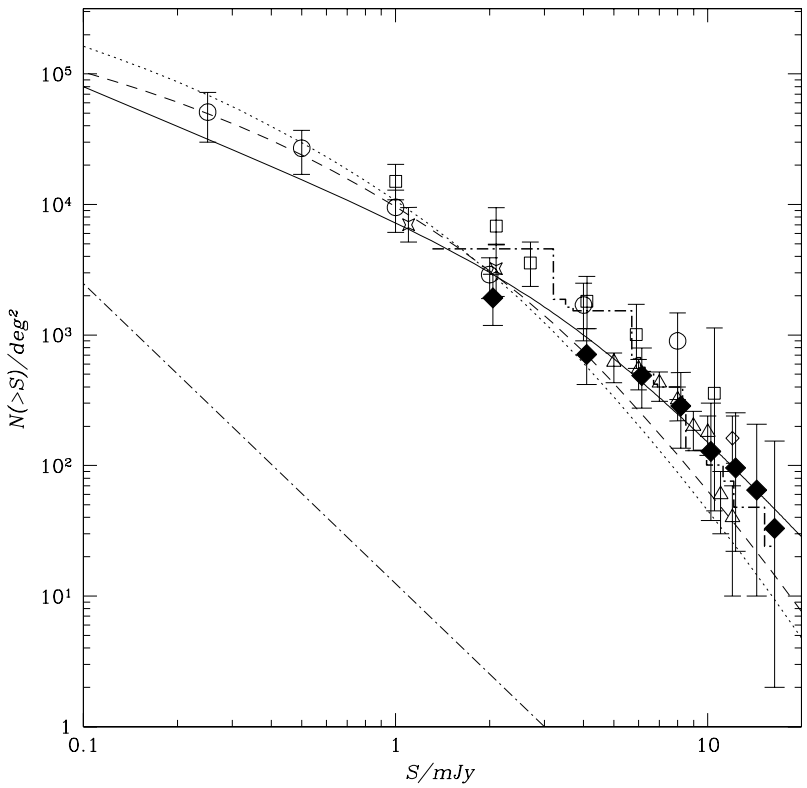

Figure 11. The 850-μm cumulative source counts. The solid diamonds denote the results from the current work. The step-function shows counts derived from the same data, but using a different recipe (see Section 6.1). Counts derived from cluster studies by Chapman et al. (2002b) and Smail et al. (2002) are shown by the open squares and circles, respectively. The UK 8-mJy survey counts Scott et al. (2002) are shown as open triangles. Stars represent the counts from Hughes et al. (1998), and the open diamond is from Borys et al. (2002). Some points are slightly offset along the flux axis for clarity. Overlaid is the two power-law model used in the calculation of γ (solid line), and two predictions based on representative galaxy evolution models from Rowan-Robinson (2001) – the dashed line represents a universe with $\Omega_{\rm M} = 1.0$ and $\Omega_\Lambda = 0.0$ while the dotted line is $\Omega_{\rm M} = 0.3$ and $\Omega_\Lambda = 0.7$. The dot-dashed line below the curves is the count prediction obtained from extrapolating the *IRAS* 60-μm counts and invoking no evolution.

this survey and the UK 8-mJy project are slightly lower than those found from surveys of smaller areas, which often involve the modelling of cluster lenses (Chapman et al. 2002b; Cowie, Barger & Kneib 2002; Smail et al. 2002). Comparing the ratio of counts derived from our survey relative to the 8-mJy project yields a factor of ∼0.85 for the 6–12 mJy range. If we fit to the average of the cluster counts and interpolate across this same range, this ratio between our counts and theirs is roughly 0.4. This might indicate that those surveys had been sensitive to clustering, which would naturally lead to an overestimate of the number counts. It could also be that the cluster lens surveys were contaminated by sources intrinsic to the clusters, or that there was some systematic bias in the lens models. We also note that some of the surveys include candidates detected with a significance lower than the 4σ cut we used here.

Although the current survey is limited by the lack of bright sources in the HDF, it is clear that the counts fall off quite steeply with increasing flux. Different surveys are often compared via the slope of a power-law form of the number counts [$N(S)\,\mathrm{d}S \propto S^{-\alpha}$]. For our counts we obtain $\alpha = 2.9 \pm 0.5$ (95 per cent confidence limits), which is in excellent agreement with estimates obtain by other groups: 2.8 ± 0.7 from Blain et al. (1999a), $3.2^{+0.7}_{-0.6}$ from Barger, Cowie & Sanders (1999) and 3.2 ± 0.7 from Eales et al. (2000).

At the faint end, it seems that the counts turn over and flatten out with decreasing flux. Indeed, if they do not then the submillimetre background will be overproduced. Deeper surveys that reach to lower flux levels will be needed in order to determine this unambiguously.

6.2 The 450-μm number counts

Since we have only detected five objects at 450 μm, we choose to quote only a single value for $N(>100$ mJy). Because the number counts are not well constrained at all at 450 μm it is difficult to know what model to use in the completeness simulations. We chose a simple power-law form with $N(S)\,\mathrm{d}S \propto S^{-\alpha}$. Our estimates of the detectability were largely insensitive to the choice of α, and turned out to be simply the inverse of the completeness at 100 mJy (80 per cent). This result, along with two previous estimates at lower fluxes, is given in Table 4. There are no published estimates at the bright flux levels which are probed here.

A fit to a power law with these combined counts gives $\alpha = 2.2 \pm 0.4$. This is not too dissimilar from the 850-μm slope, though slightly shallower. This might be an interesting result: if the SCUBA sources are mainly at $z \gtrsim 1$, then one would expect the 450-μm fluxes to drop off more steeply than the 850-μm counts because the K-correction becomes positive for 450 μm at these redshifts. With only three estimates for the 450-μm number counts, however, it is premature to draw strong conclusions. Nevertheless, this shows that constraints on the number counts at different wavelengths can serve as a probe of the evolution and redshift distribution of submillimetre galaxies.

Table 4. 450-μm source counts from the HDF super-map. We present here our estimate and those compiled from the literature. The other estimates are based on a different approach and also chose to quote symmetric error bars.

Flux (mJy)	$N(>S)$	Comment
10	2100^{+1200}_{-1200}	Smail et al. (2002)
25	500^{+500}_{-500}	Smail et al. (2002)
100	140^{+160}_{-90}	This work

7 CLUSTERING OF SUBMILLIMETRE SOURCES

As we have already mentioned, the presence of clustering may also affect estimates for the source counts. Peacock et al. (2000) report weak evidence of clustering in the $\sim 2 \times 2$ arcmin^2 map of H98 in the sense of statistical correlations with LBGs, which are themselves strongly clustered (Giavalisco & Dickinson 2001). The UK 8-mJy survey (Scott et al. 2002), which covers over 250 arcmin^2, and the smaller yet deeper CFRS 3- and 14-h fields (Webb et al. 2003) fail to detect clustering among the SCUBA-detected sources. There appears (by eye) to be clustering in the super-map; in particular the concentration of sources near the centre of the map, the trio of sources to the west of the map, and the group of four north of it might suggest a clustering scale on the order of 30 arcsec or so. However, one would *expect* more sources in these areas because of the increased sensitivity. Hence one needs to carry out a statistical clustering analysis, including the inhomogeneous noise, to quantify this.

Clustering is usually described as the probability, p, of finding a source in a solid angle Ω, and another object in another solid angle Ω separated by an angle θ. This probability is described by

$$p(\theta) = N^2[1 + w(\theta)]\Omega^2, \tag{5}$$

where N is the mean surface density of objects on the sky and $w(\theta)$ is the angular two-point correlation function. If $w(\theta)$ is zero, then the distribution of sources is completely random, while otherwise it describes the probability in excess of random. The correlation function $w(\theta)$ is estimated by counting pairs and there are several specific estimators in the literature. The one we employ is that proposed by Landy & Szalay (1993):

$$w(\theta) = \frac{DD - 2DR + RR}{RR}, \tag{6}$$

with

$$\delta w(\theta) = \sqrt{\frac{1 + w(\theta)}{DD}}. \tag{7}$$

This particular estimator has been shown to have no bias and also has a lower variance than the alternatives. In this equation, D represents sources in the SCUBA catalogue, and R are sources recovered from Monte Carlo catalogues. DD is the number of pairs of real sources that fall within a bin of width $\delta\theta$ in the map. DR are data–random pairs and RR are random–random. For simplicity, each catalogue is normalized to have the same number of objects. To obtain the random catalogues, we created 1000 mock fields based on the source count model used in the previous section, and the actual noise of the real data. The sources were placed randomly throughout the field, and the resulting mock data were placed into the same pipeline as our real data.

This approach is slightly different from that of Webb et al. (2003) and Scott et al. (2002), the only other two surveys to attempt a clustering analysis of SCUBA sources. In those analyses, the mock images were modified only by adding noise to each pixel. The amount of noise added was taken from the noise map which was created along with the real signal map. Therefore, their final mock images do not exhibit the chop pattern that one would expect to see. Recognizing this limitation, Webb et al. (2003) took the added step of masking out regions in the mock images that correspond to the positions of the off-beams in the real map. Our simulations involve a

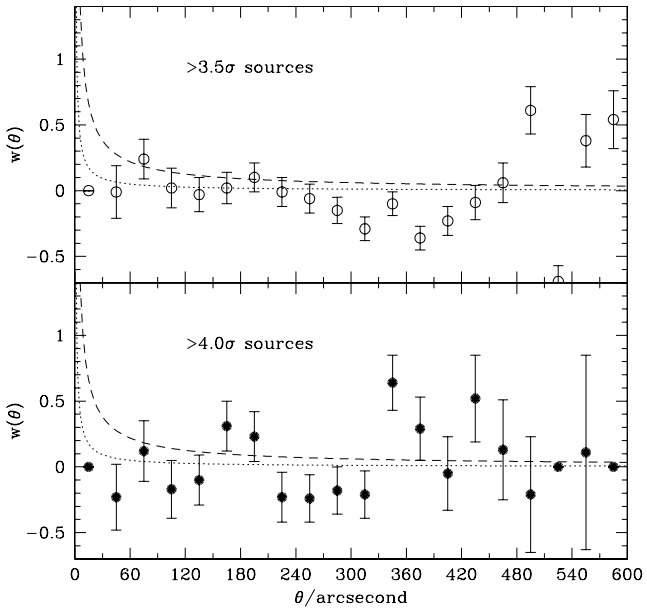

Figure 12. Angular two-point correlation function estimate for the HDF super-map sources. Our estimates of $w(\theta)$ are shown as the open circles (for the $> 3.5\sigma$ catalogue) and filled circles (for the $> 4.0\sigma$ catalogue). The points are plotted at the mid-point of each 30-arcsec bin. The first point is zero because there are no objects in the super-map closer than 30 arcsec to another. The measured clustering signal of EROs is shown as a dashed line and that of LBGs as a dotted line. There is no evidence of submillimetre clustering here, though the errors are still quite large.

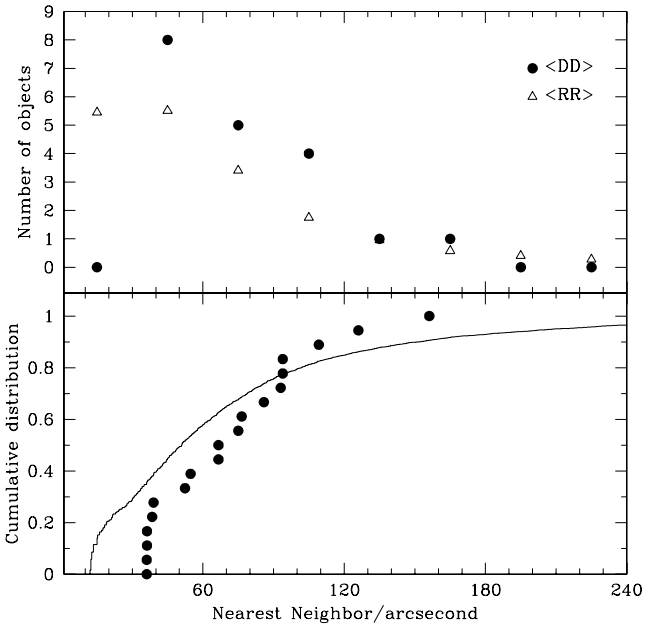

Figure 13. Nearest-neighbour clustering analysis. In the top panel we plot the nearest-neighbour distribution of the data compared with a Monte Carlo generated random set. The random data falls off below 12 arcsec, where our source extractor is unable to separate unique objects. There is a lack of real sources detected with pair separations less than ∼30 arcsec. This is also reflected in the bottom panel, where we plot the cumulative distribution of nearest neighbours (dots) compared with Monte Carlo simulations (solid line).

full sampling of the mock images using the astrometry information from the real data. Therefore, the simulated and real maps have the same beam features.

We used relatively wide 30-arcsec bins because the number of sources is so low. This is also twice the size of the SCUBA beam at 850 μm, which was the bin size criterion used by Scott et al. (2002). $w(\theta)$ is estimated using both the 3.5σ and 4σ catalogues. Though some of the 3.5σ sources may be spurious, the increased number of objects helps bring down the clustering error bars. As Fig. 12 shows, however, even when the 3.5σ sources are included there is no evidence for clustering in the HDF super-map, since there is no angular bin that has a $w(\theta)$ significantly different from zero. For comparison in that figure, we also plot estimates of $w(\theta)$ for EROs and LBGs (Daddi et al. 2000; Giavalisco & Dickinson 2001). We repeated this using bins half as wide, and again no significant deviation from zero was found.

This is not the only clustering estimator one can use. We also performed a 'nearest-neighbour' analysis (see, e.g., Scott & Tout 1989) to test whether sources were closer together than expected at random. This statistic simply examines the distribution of distances to the nearest neighbours for each source. The cumulant of nearest neighbours is then compared against our set of Monte Carlo catalogues to determine if a pairwise clustering signal is present. The results are shown in Fig. 13.

There is a lack of sources with neighbours closer than ∼30 arcsec, but a formal Kolmogorov–Smirnov test indicates only a ∼40 per cent chance that the distributions are significantly different. So there is no strong evidence of clustering here either.

Note that in each of these clustering analyses, it is difficult to estimate the clustering strength on scales near to the beam size. Our source extraction algorithm is insensitive to a fainter source closer than 12 arcsec to a brighter one. Note that if SCUBA sources are clustered in a similar manner as EROs or LBGs, then the signal in $w(\theta)$ would be expected to be strongest at $\lesssim$30 arcsec. This is only a factor of 2 larger than the SCUBA beam, and therefore one expects that a clustering detection with SCUBA will be rather difficult due to blending of the sources. Our particular approach has not been optimized for separating nearby sources and hence our catalogue is not ideal for clustering analysis. Future attempts to measure the clustering strength should pay particular care to source extraction algorithms.

There is currently no convincing detection of submillimetre clustering; what is needed is a very large (∼1 deg^2) survey with hundreds of sources in order to decrease the error bars on the clustering estimate. The on-going SHADES survey (see http://www.roe.ac.uk/ifa/shades/) purports to do just that.

8 IMPLICATIONS OF THE COUNTS

8.1 The 850-μm submillimetre background

We explored the range of parameters for the two-parameter model that could fit our source counts and still fall within the limits of the FIR 850-μm background constraint: 3.1–4.1 × 10^4 mJy deg^{-2} (Puget et al. 1996; Fixsen et al. 1998; Hauser et al. 1998). By calculating the integral of $SN(S)\,\mathrm{d}S$ we find that our >2 mJy sources contribute 1.4 × 10^4 mJy deg^{-2} to the FIR background (FIB). This is consistent with estimates from several groups, and demonstrates that a significant fraction of the submillimetre Universe is still below the flux threshold attainable from current SCUBA surveys. However, given the freedom which still exists in the faint end counts, and in the current level of uncertainty of the submillimetre background itself, the entire background can easily be made up of sources with

$S_{850\,\mu m} > 0.1$ mJy. This result can be used to constrain models that predict the evolution of IR luminous galaxies. Future surveys that detect more sources will constrain the source counts further, and extend the limiting flux down to fainter levels.

8.2 Evolution of submillimetre sources

The counts are much greater than what one obtains by estimating 850-μm fluxes simply from the *IRAS* 60-μm counts. As addressed by Blain et al. (2002), a SCUBA galaxy with a flux $\gtrsim$5 mJy has an inferred luminosity in excess of 10^{12} $L_\odot$ if they are distributed at redshifts greater than 0.5. Note that Chapman et al. (2003) find spectroscopic redshifts $z > 0.8$ for each source in their sample of SCUBA-detected radio galaxies. Such sources make up at least 50 per cent of the SCUBA population brighter than 5 mJy, and radio-*undetected* sources are likely to be at even higher redshifts.

At these luminosities the number of SCUBA objects per comoving volume is several hundred times greater than it is today. Therefore, there must be significant evolution past $z \gtrsim 0.3$ (the *IRAS* limiting redshift).

Modelling this evolution has been difficult due to the lack of observational data on the redshift distribution of SCUBA sources. Attempts to model the luminosity evolution of the SCUBA sources have been carried out using semi-analytic methods (e.g. Guiderdoni et al. 1998) and parametric ones (e.g. Blain et al. 1999a; Rowan-Robinson 2001; Chapman et al. 2003). In many cases, the starting point is the well-determined *IRAS* luminosity function. This gives us the number of sources of a given luminosity per comoving volume. These luminosities are then modified as a function of redshift, and then 850-μm fluxes are extrapolated and source counts determined. We expect the number of galaxies to increase in the past due to merger activity, so number evolution must play some role, but it is noted that strong number evolution overproduces the FIR background. There are many models (and a range of parameters within them) that fit the current data. Therefore, until we can better constrain the counts and determine redshifts, the only firm conclusion one can make is that SCUBA sources do evolve strongly. Our catalogue of 34 SCUBA sources within the HDF region, with the amount of multiwavelength data being collected there, should contribute toward distinguishing between models.

8.3 A connection with modern-day elliptical galaxies?

Observations of local star-forming galaxies suggest that

$$\mathrm{SFR} = 2.1 \times 10^{-10} (L_{60\,\mu m}/L_\odot)\, M_\odot\ \mathrm{yr}^{-1}, \quad (8)$$

where $L_{60\,\mu m} \equiv (\nu S_\nu)|_{60\,\mu m}$ is the 60-μm luminosity (Rowan-Robinson et al. 1997). Assuming the SLUGS result for dust temperature and emissivity (Dunne et al. 2000), we calculate star formation rates (SFRs) in excess of 1000 $M_\odot$ yr^{-1} for redshifts past approximately 1. Of course the conversion between detected flux and inferred star formation rate is highly dependent on the dust spectral energy distribution (SED), and can change by factors of 10 for changes in temperature and β of only 2. Also, the simple relation between FIR luminosity and SFR may be different for these more luminous sources (Thronson & Telesco 1986; Rowan-Robinson et al. 1997).

Despite these uncertainties, it has been suggested (e.g. Blain et al. 2002 and references therein) that SCUBA sources can be associated with the elliptical galaxies we see today via the following argument. Producing the local massive elliptical population with a homogeneous stellar distribution requires a sustained period of star formation on the order of 1000 $M_\odot$ yr^{-1} lasting approximately 1 Gyr. Based on results from Chapman et al. (2003) that place the bright SCUBA population at $z > 1$, the number of these galaxies per unit comoving volume is comparable to the density of the local elliptical population. For example, if we take our estimate of the counts above *5* mJy and assume that they cover a redshift range between 2 and 4 in a standard flat Λ-dominated model, we obtain a density of approximately 7×10^{-5} $(h^{-1}\ \mathrm{Mpc})^{-3}$. These are thus rare and extremely luminous objects, with comparable number densities to galaxy clusters or quasars.

If SCUBA sources really are associated with elliptical galaxies, they should exhibit spatial clustering like their local counterparts. There are other reasons one might expect detectable clustering; Extremely red objects (EROs) are very strongly clustered (Daddi et al. 2000), and seem to have a correlation with SCUBA sources. In general, objects associated with major mergers should show high-amplitude clustering (e.g. Percival et al. 2003).

Although our analyses show no sign of clustering, the data are not powerful enough to rule it out. To improve on this we need more detected sources in order to bring down the Poisson error bars. Also, the ERO and LBG clustering observations are taken from samples that exist at a common redshift (∼1 in the case of EROs and ∼3 for LBGs). Because of the strong negative *K*-correction, detected SCUBA sources are spread across a much wider redshift range, therefore diluting the clustering signal. Hence, progress can only be made with a larger survey (such as SHADES) that also has the ability to discriminate redshifts, even if only crudely.

Although more studies are required to verify this claim, it is a reasonable hypothesis, and one with some testable predictions. Our new catalogue of SCUBA sources (Table 2) should allow for future detailed comparison with other wavelength data, which facilitate such tests.

9 CONCLUSIONS

This paper has presented the most complete accounting of submillimetre flux in the HDF-North region to date. We were able to demonstrates that $>4\sigma$ SCUBA detections are quite robust, being consistently detected in independent observations of the same area. Our catalogue of sources was obtained using a careful statistical approach, involving simulations with the same noise properties as the real data. At 850 μm we were able to extract 19 sources above 4σ and a further 15 likely sources above 3.5σ. Such a large list, in a field with so much multiwavelength data, should be extremely useful for further studies.

Our estimated source counts cover a wider flux density range than any other estimates, and given the careful completeness tests we carried out, they are likely to be more reliable than combining counts from different surveys. Our counts of SCUBA sources verify that significant evolution of the local LIRG population is required. Extrapolating a fit to these counts to below *2* mJy can reasonably recover the entire FIB at 850 μm. Clustering, although anticipated to be strong, was not detected in our map, due largely to the limited number of sources. Several hundred submillimetre sources with at least some redshift constraint will be required to detect the clustering unambiguously.

The power of the SCUBA observations in the HDF-N lies not in the detection of objects per se, but rather for the ability to compare them with the plethora of existing and upcoming deep maps of this region at a wide variety of other wavelengths. Some of these comparisons will be the focus of Paper II.

ACKNOWLEDGMENTS

This work was supported by the Natural Sciences and Engineering Research Council of Canada. The James Clerk Maxwell Telescope is operated by The Joint Astronomy Centre on behalf of the Particle Physics and Astronomy Research Council of the United Kingdom, the Netherlands Organization for Scientific Research, and the National Research Council of Canada. Much of the data for this paper was obtained via the Canadian Astronomy Data Centre, which is operated by the Herzberg Institute of Astrophysics, National Research Council of Canada. We also thank Amy Barger for access to some of her data prior to their release in the public archive.

NOTE ADDED IN PROOF

After this paper went to press, new SCUBA observations by Wang et al. (private communication) failed to detect three sources from our 4σ catalogue (Table 2). The sources, SMMJ123607+621145, SMMJ123608+621251 and SMMJ123621+621254, were imaged primarily using the scan-map mode of SCUBA. However, the first two were also sampled by our own group (project M00BC01, as mentioned in Table 1) using the jiggle-map mode, indicating two sources offset from the scan-map positions and at roughly two-thrids the reported flux. Further investigation has determined that these data were obtained while the source was near transit, where it is known that the JCMT had difficulty pointing, and indeed the logs reveal that a shift of over 8 arcsec was required part-way through the data collection. Given the difficulty in interpreting the data under these circumstances, we chose not to include these jiggles in the analysis described in this paper. The new data collected by Wang & Cowie (private communication) is deep, does not suffer from these same problems, and should detect the sources if they are real. Unfortunately, we have discovered that these data contain a noise artifact (at the jiggle frequency) which complicates their interpretation. Hence we caution that the reality of those particular sources is currently difficult to establish, although this would not significantly affect any of the conclusions of our paper. The HDF-N submm map is being expanded by several groups in order to match the anticipated *SIRTF* coverage, and therefore future work will revisit the sources described here, including these three in question.

REFERENCES

Archibald E.N. et al., 2002, MNRAS, 336, 1
Barger A.J., Cowie L.L., Sanders D.B., 1999, ApJ, 518, L5
Barger A.J., Cowie L.L., Richards E.A., 2000, AJ, 119, 2002 (Ba00)
Blain A.W., Kneib J.-P., Ivison R.J., Smail I., 1999a, ApJ, 512, L87
Blain A.W., Smail I., Ivison R.J., Kneib J.-P., 1999b, MNRAS, 302, 632
Blain A., Smail I., Ivison R.J., Kneib J.-P., Frayer D.T., 2002, Phys. Rep., 369, 111
Borys C., 2002, PhD thesis, Univ. British Columbia
Borys C., Chapman S.C., Halpern M., Scott D., 2002, MNRAS, 330, L63 (Bo02)
Borys C., Chapman S.C., Halpern M., Scott D., 2003, MNRAS, submitted
Chapman S.C. et al., 2000, MNRAS, 319, 318
Chapman S.C., Lewis G.F., Scott D., Borys C., Richards E., 2002a, ApJ, 570, 557
Chapman S.C., Scott D., Borys C., Fahlman G.G., 2002b, MNRAS, 330, 92
Chapman S.C., Helou G., Lewis G.F., Dale D.A., 2003, ApJ, 588, 186
Cowie L.L., Barger A.J., Kneib J.-P., 2002, AJ, 123, 2197
Daddi E., Cimatti A., Pozzetti L., Hoekstra H., Röttgering H.J.A., Renzini A., Zamorani G., Mannucci F., 2000, A&A, 361, 535
Dunne L., Eales S., Edmunds M., Ivison R., Alexander P., Clements D.L., 2000, MNRAS, 315, 115
Eales S., Lilly S., Webb T., Dunne L., Gear W., Clements D., Yun M., 2000, AJ, 120, 2244
Eddington A.S., 1940, MNRAS, 100, 354
Ferguson H.C., Dickinson M., Williams R., 2000, ARA&A, 38, 667
Fixsen D.J., Dwek E., Mather J.C., Bennett C.L., Shafer R.A., 1998, ApJ, 508, 123
Giavalisco M., Dickinson M., 2001, ApJ, 550, 177
Guiderdoni B., Hivon E., Bouchet F.R., Maffei B., 1998, MNRAS, 295, 877
Hauser M.G. et al., 1998, ApJ, 508, 25
Holland W.S. et al., 1999, MNRAS, 303, 659
Hughes D.H. et al., 1998, Nat, 394, 241 (H98)
Jenness T., Lightfoot J.F., 1998, ASP Conf. Ser. Vol. 145, Astronomical Data Analysis Software and Systems VII, 7. Astron. Soc. Pac., San Francisco, p. 216
Johnstone D., Wilson C.D., Moriarty-Schieven G., Giannakopoulou-Creighton J., Gregersen E., 2000, ApJs, 131, 505
Landy S.D., Szalay A.S., 1993, ApJ, 412, 64
Peacock J.A. et al., 2000, MNRAS, 318, 535
Percival W.J., Scott D., Peacock J.A., Dunlop J.S., 2003, MNRAS, 338, L31
Puget J.-L., Abergel A., Bernard J.-P., Boulanger F., Burton W.B., Desert F.-X., Hartmann D., 1996, A&A, 308, L5
Richards E.A., 2000, ApJ, 533, 611
Rowan-Robinson M., 2001, ApJ, 549, 745
Rowan-Robinson M. et al., 1997, MNRAS, 289, 490
Scott D., Tout C.A., 1989, MNRAS, 241, 109
Scott S.E. et al., 2002, MNRAS, 331, 817
Serjeant S. et al., 2003, MNRAS, in press (S02) (astro-ph/0201502)
Smail I., Ivison R.J., Blain A.W., 1997, ApJ, 490, L5
Smail I., Ivison R.J., Blain A.W., Kneib J.-P., 2002, MNRAS, 331, 495
Thronson H.A., Telesco C.M., 1986, ApJ, 311, 98
Webb T.M.A., Eales S.A., Lilly S.J., Clements L., Dunne L., Gear W.H., Flores H., Yun M., 2003, ApJ, 587, 41
Williams R.E. et al., 1996, AJ, 112, 1335

This paper has been typeset from a TEX/LATEX file prepared by the author.